

Validation of Monte Carlo ^{131}I radiopharmaceutical dosimetry workflow using a 3D printed anthropomorphic head and neck phantom

David P. Adam¹, Joseph Grudzinski², Ian Bormett³, Benjamin L. Cox³, Ian R. Marsh¹, Tyler J. Bradshaw², Paul Harari⁴, Bryan Bednarz^{1a}

¹⁾ Department of Medical Physics, University of Wisconsin-Madison, Madison, WI, 53705

²⁾ Department of Radiology, University of Wisconsin-Madison, Madison, WI, 53705

³⁾ Morgridge Institute for Research, University of Wisconsin-Madison, Madison, WI, 53705

⁴⁾ Department of Human Oncology, University of Wisconsin-Madison, Madison, WI, 53705

^{a)} Author to whom correspondence should be addressed.

To Medical Physics

Grant support: This project was partially supported by the Morgridge Institute for Research, the Specialized Program of Research Excellence (SPORE) program, through the NIH National Institute for Dental and Craniofacial Research (NIDCR) and National Cancer Institute (NCI), grant P50DE026787, the National Cancer Institute (NCI) Research Project-Cooperative Agreements U01CA233102-01, and the NIH National Cancer Institute (NCI), grant P01CA250972.

Corresponding author: Bryan P. Bednarz, Department of Medical Physics, 1005 WIMR, 1111 Highland Avenue, Madison WI 53705; +1-608-262-5225; bbednarz2@wisc.edu

First author: David P. Adam (graduate student), Department of Medical Physics, 1005 WIMR, 1111 Highland Avenue, Madison WI 53705; +1-(608) 265-6116; dadam@wisc.edu

Word Count: 5411 (excluding references)

Running title: ^{131}I anthropomorphic phantom dosimetry

Abstract

Purpose:

Approximately 50% of head and neck cancer (HNC) patients will experience loco-regional disease recurrence following initial courses of therapy. Retreatment with external beam radiotherapy (EBRT) is technically challenging and accompanied by a significant risk of irreversible damage to normal tissues. Radiopharmaceutical therapy (RPT) is a potential method to treat recurrent HNC in conjunction with EBRT. Phantoms are used to calibrate and add quantification to nuclear medicine images and anthropomorphic phantoms can account for both the geometrical and material composition of the head and neck. In this study, we present the creation of an anthropomorphic, head and neck, nuclear medicine phantom and its characterization for the validation of a Monte Carlo, SPECT image based, ^{131}I RPT dosimetry workflow.

Methods:

3D printing techniques were used to create the anthropomorphic phantom from a patient CT dataset. Three ^{131}I SPECT/CT imaging studies were performed using a homogeneous, Jaszczak, and an anthropomorphic phantom to quantify the SPECT images using a GE Optima NM/CT 640 with a high energy general purpose (HEGP) collimator. The impact of collimator detector response (CDR) modeling and volume-based partial volume corrections (PVC) upon the absorbed dose was calculated using an image based, Geant4 Monte Carlo RPT dosimetry workflow and compared against a ground truth scenario. Finally, uncertainties were quantified in accordance with recent EANM guidelines.

Results:

The 3D printed anthropomorphic phantom was an accurate re-creation of patient anatomy including bone. The extrapolated Jaszczak recovery coefficients were greater than that of the 3D printed insert (~22.8 ml) for both the CDR and non-CDR cases (with CDR: 0.536 vs. 0.493, non-CDR: 0.445 vs. 0.426 respectively). Utilizing Jaszczak phantom PVCs, the absorbed dose was underpredicted by 0.7% and 4.9% without and with CDR, respectively. Utilizing anthropomorphic phantom RCs overpredicted the absorbed dose by 3% both with and without CDR. All dosimetry scenarios that incorporated PVC were within the calculated uncertainty of the activity. The uncertainties in the cumulative activity ranged from 25.6% to 113% for Jaszczak spheres ranging in volume from 0.5 ml to 16 ml.

Conclusion:

The accuracy of Monte Carlo-based dosimetry for ^{131}I RPT in head and neck cancer was validated with an anthropomorphic phantom. In this study, it was found that Jaszczak based PVC were sufficient. Future applications of the phantom could involve 3D printing and characterizing patient specific volumes for more personalized RPT dosimetry estimates.

Keywords: Monte Carlo, radiopharmaceutical therapy, dose calculation, anthropomorphic phantom, SPECT, 3D Printing

1. Introduction

Approximately 50% of head and neck cancer (HNC) patients will experience loco-regional disease recurrence following initial courses of therapy¹⁻⁶. Although a majority of patients can be cured from HNC, the 5 year overall survival rate of patients with locally advanced and/or recurrent HNC is approximately 50-60%⁷ and cure rates have improved only marginally over the last 30 years⁸. Retreatment of HNC is technically challenging and accompanied by a significant risk of irreversible damage to normal tissues that can translate into profound adverse effects on patient health-related quality of life^{9,10,19-21,11-18}. Several studies have ascertained that, despite improvement in long term survival (2 years) in approximately 10-20% of recurrent HNC patients following external beam radiation therapy (EBRT), there is considerable risk for high-grade toxicities after treatment^{9,10,19-22,11-18}. Despite the ability of EBRT to provide disease control, efforts to reduce the potential of acute and long-term tissue injury in locoregionally recurrent HNC patients following EBRT are clearly warranted.

Radiopharmaceutical therapy (RPT) is one potential treatment that can be combined with EBRT to maintain disease control of recurrent HNC and mitigate high-grade toxicities. RPT involves a biological delivery vector labeled with a radioactive isotope that is designed to preferentially attach to or be internalized by cancer cells. The radioactive drug conjugate is infused directly into a patient's bloodstream allowing it to reach tumor sites located throughout the body. Due to this unique delivery route, the dose limiting organs are different than EBRT; and, when combined with EBRT, the therapeutic window in the patient can be expanded, allowing physicians to treat more aggressively.

CLR 131²³, an alkyl phosphocholine (APC) analog with broad cancer targeting abilities, is a promising RPT agent paired to the radioisotope ¹³¹I, which emits both therapeutic beta particles (mean energy of 606 keV) and diagnostic gamma rays (364 keV) which can be localized using SPECT. APCs enter cells through specialized plasma membrane microdomains called lipid rafts²³, which are expressed 6-10 times more in cancer cells in comparison to normal tissues. The increased specificity of CLR 131 for malignant cells has led to increased therapeutic efficacy in both preclinical and clinical studies. Preclinical studies confirm preferential uptake and retention of CLR 131 in murine HNC xenografts and tumor growth inhibition²⁴. Tumor targeting has been observed in patients in on-going and completed clinical trials²⁵⁻²⁷. Additional tumor growth inhibition has been demonstrated when CLR 131 is combined with EBRT²⁴.

Given these results, a clinical trial (NCT04105543) is underway at UW-Madison to investigate the efficacy of combining CLR 131 with EBRT with curative intent in treating relapsed HNC²⁸.

The premise of the trial is to evaluate the combination of CLR 131 and EBRT in the treatment of recurrent HNC wherein the radiation dose deposited by the CLR 131 permits a dose reduction delivered by EBRT (e.g., standard of care 60-70 Gy will be targeted irrespective of radiation modality). The overall hypothesis of the clinical trial is that the addition of CLR 131 will support a dose reduction of EBRT which will be safe and tolerable while maintaining favorable tumor response rates and diminishing the adverse impact of radiation treatment on subject specific symptoms, such as quality of life, salivary flow and swallowing function.

To achieve the objectives of the trial ²⁹, patient-specific dosimetry is needed to accurately characterize the tumor absorbed dose from CLR 131 on the voxel level. Longitudinal SPECT/CT [31] scans are used to map the time-dependent biodistribution of CLR 131 in the patient and serve as the input for voxel-level dosimetry calculations performed by an in-house Monte Carlo-based software called RAPID ³⁰. The accuracy of the CLR 131 dose calculation depends on the quantitative accuracy of ¹³¹I SPECT images. Nuclear medicine phantom scans are used both for quantitative calibration (i.e. convert counts to units of activity) and correction of partial volume effects (PVE). PVEs, which are dependent on both the size and shape of the structure being imaged ³¹⁻³³, are caused by inherent resolution limitations of imaging systems and can significantly degrade SPECT/CT image quality and quantitative accuracy.

Collimator detector response (CDR) modeling has been recommended by MIRD pamphlet 24 ³⁴ for SPECT image reconstruction due to septal penetration of high energy ¹³¹I photons through the collimator. Without CDR modeling, noise can be quite apparent on reconstructed images and small structures can be difficult to resolve; however, some have observed Gibbs ringing artifacts on images reconstructed with CDR enabled which can affect the resultant activity distribution ³⁵.

Anthropomorphic nuclear medicine phantoms have been investigated for a variety of organs (kidney ³⁶⁻³⁹, liver ^{37,39-41}, spleen ^{37,39}, and pancreas^{37,38}), but few groups have investigated the use of nuclear medicine head and neck phantoms. 3D printed head and neck phantoms have been created for CT and MR applications but few for nuclear medicine applications. A prototype head and neck phantom was described by Alqahtani et. al in which the performance of gamma imaging systems was evaluated but the study did not extend to dosimetry ⁴². In these studies, results have generally indicated that anthropomorphic phantoms account for heterogeneities that are not present in traditional nuclear medicine phantoms and are often more accurate than non-anthropomorphic phantoms. 3D printed anthropomorphic head and neck phantoms that account for the changing contour of the head and neck region and the heterogeneous material composition in the patient have not been investigated. A couple of recently published review articles succinctly demonstrate the state of 3D printed phantoms ^{43,44}.

In this work we aim to validate our image based RPT dosimetry workflow for the HNC clinical trial with the introduction and characterization of a novel, 3D printed, anthropomorphic, head and neck nuclear medicine phantom that mimics the geometry and material composition of the head and neck region. Imaging studies will be conducted with both traditional Jaszczak nuclear medicine phantoms and the anthropomorphic phantom to investigate ^{131}I SPECT/CT calibration, partial volume corrections (PVCs), and the role of collimator detector response (CDR) modeling on dosimetry. The resultant data from the imaging studies will then be used as input for the ^{131}I RPT dosimetry workflow and compared to ground truth scenarios. Finally, the uncertainties from the imaging studies will be investigated and the impact of uncertainties on the dosimetry will be discussed.

2. Methods

2.1 Phantom Creation

The original CT data for the anthropomorphic phantom was accessed from a publicly available database provided by Radiation Therapy Oncology Group (RTOG) 0522 study (**Figure 1a**)⁴⁵. The CT data had a voxel resolution of $0.98 \times 0.98 \times 2.4 \text{ mm}^3$. Important structures such as the tumor, thyroid, lacrimal glands (both left and right), parotid glands (both left and right), and bone were contoured manually using Amira v.5.3.3 (**Figure 1b**). The labels were then converted to .stl files, which is a file format native to the stereolithography CAD software created by 3D systems and required for 3D printing. The .stl files were then modified for final assembly using Magics (Materialise NV, Leuven, Belgium), which is an .stl editing software package (**Figure 1c,d**). Modifications included the addition of flanges to seal the main volume, the incorporation of mounting points for the assembly of bones and other anatomical features, and ports for filling and sealing the tumor and gland voids.

The final phantom design consisted of nine custom parts, along with commercial hardware for assembly. This included seven 3D printed pieces, made with two different materials, and two laser-cut acrylic plates. The main chamber (skin) was printed using stereolithography (SL) out of Accura60, a proprietary photopolymer resin (3D Systems, Rock Hill, SC, USA), and then clear-coated for water resistance. The thyroid gland was fused to the skin and can be filled independently. The skull and spine were split into three separate parts and printed using SL out of Somos PerFORM, a proprietary photopolymer resin (DSM, Heerlen, Netherlands). The lacrimal glands were fused to the front piece of the skull and can be filled independently. Lastly, the parotid voids and tumor void were printed using SL out of Accura60 (3D Systems). The top and bottom of the chamber were formed with quarter inch acrylic plates that were laser-cut to their

final size with a PLS6.75 Laser Cutting System (Universal Laser Systems, Scottsdale, AZ, USA). Commercial hardware included o-rings for sealing and nylon bolts for assembly of separate components. The final 3D printed head-and-neck anthropomorphic phantom is shown in **Figure 1e** and a sagittal slice of a CT image of the phantom is depicted in **Figure 1f**. **Table 1** shows the physical material properties taken from material datasheets of the Accura60 and Somos PerFORM comprising the phantom.

Table 1: Physical properties of the bulk materials

Material	Tensile strength (MPa)	Elongation at break (%)	Tensile Modulus (MPa)	Flexural strength (MPa)	Water absorption (%)	Hardness (Shore D)
Accura60	58-68	5-13	2690 - 3100	87-101	N/A	86
Somos PerFORM	68-80	1.1-1.2	9800 - 10500	120-146	0.1-0.2	93-94

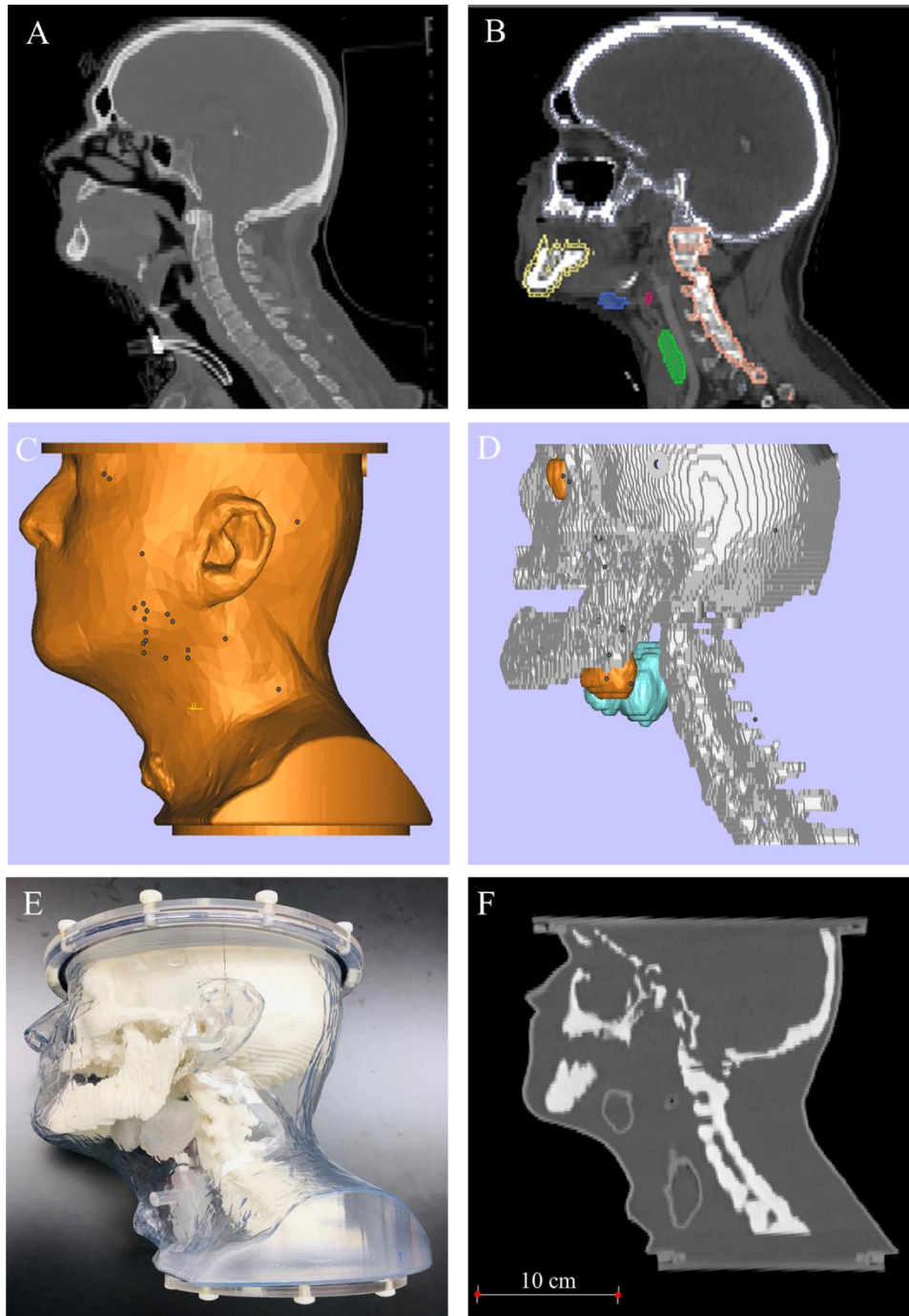


Figure 1: Representation of the H&N anthropomorphic phantom development process. (a) Original CT image obtained from a RTOG managed publicly available image repository and (b) relevant contoured structures. (c-d) 3D rendering of patient's skin, bony anatomy, and fillable organ anatomies. (e) Final 3D printed H&N anthropomorphic phantom. (f) CT image of H&N anthropomorphic phantom.

2.2 Phantom studies and SPECT/CT image acquisition

Three phantom studies were conducted, the parameters of which are summarized in **Table 2**. The first was conducted using a uniform 20 cm cylindrical phantom of volume 5.64 L to calculate the calibration factor to convert the reconstructed SPECT images to units of activity concentration. The second study was with a Jaszczak phantom containing 0.5-, 1-, 2-, 4-, 8-, and 16-ml hollow sphere inserts, with corresponding diameters of 9.9, 12.4, 15.4, 19.8, 24.8 and 31.3 mm, injected with a 9.9:1 insert to background activity concentration and was used to calculate spherical based recovery coefficients (RC) for PVC determination. The third study was with the anthropomorphic phantom containing a 22.8 ml tumor insert and injected with a 9.9:1 insert to background activity concentration. The resultant images were used to calculate an anthropomorphic based recovery coefficient and served as the basis for the image based RPT dosimetry calculation. SPECT/CT acquisitions were conducted using a GE Optima NM/CT 640 with a high energy general purpose (HEGP) collimator. All images were acquired over 360 degrees into 128x128 pixel matrices per angle. Body contouring was enabled. A photopeak energy window centered at 364 keV and 20% in width (327.6 – 400.4 keV) and a triple energy window scatter correction with two 20% windows adjacent (267.3 – 326.7 keV and 401.4 – 490.6 keV) to the photopeak window were used in the acquisition. A CT was acquired after the SPECT acquisition for CT-derived attenuation corrections (Hawkeye CT, 120 kVp, 20 mA, 487 mAs) and for accurate determination for the location of hot spheres and tumor insert.

Raw image data was reconstructed using the GE Xeleris 4.0 ordered subset expectation maximum (OSEM) algorithm with 10 iterations and 10 subsets with CT-based attenuation correction and both with and without GE's CDR modeling named 'Resolution Recovery' (without: non-RR, with: RR). No post-reconstruction filtering was applied. The reconstructed SPECT image matrices were 128 x 128 x 128 voxels with a voxel size of 4.42 x 4.42 x 4.42 mm³ and the reconstructed CT images had a voxel size of 0.98 x 0.98 x 5.0 mm³. High-resolution CT images of the anthropomorphic phantom were also acquired using a Siemens SOMATOM Definition Edge (120 kVp, 452 mA, 226 mAs) with a voxel size of 0.977x0.977x2.0 mm³.

Table 2: Parameters used for SPECT/CT phantom studies

Study	Initial ¹³¹ I Activity Concentration (kBq/ml)	Insert to Background Ratio	Number of frames	Seconds per frame
20 cm cylindrical phantom	105	N/A	120	20
Hot sphere Jaszczak	259	9.9:1	120	60
Anthropomorphic	257	9.9:1	120	60

2.3 Calculation of calibration factor and recovery coefficients

To convert the recorded SPECT image data into units of activity, the calibration factor, Q, was calculated according to Equation (1),

$$Q = \frac{R}{V \cdot C} \cdot e^{\lambda \Delta t} \quad (1)$$

where R is the mean count rate of a voxel in a VOI, V is the volume a voxel, C is the activity concentration at the time of syringe measurement, and the last term accounts for physical decay between source preparation time and scan time (Δt).

If R_{voxel} is the count rate in a voxel, then the activity in the voxel, A_{voxel} , is given by Equation (2).

$$A_{voxel} = \frac{R_{voxel}}{Q} \quad (2)$$

To account for PVE, recovery coefficients were calculated according to Equation (3) where the measured activity concentration in the object VOI was determined by quantifying the mean value of each hot insert. Contours for the hot inserts were drawn on the CT and then the reconstructed SPECT was up-sampled using a Lanczos filter to the resolution of the CT and registered to the CT.

$$RC = \frac{\text{measured activity concentration in object VOI}}{\text{true activity concentration in object VOI}} \quad (3)$$

To correct the activity in a voxel, the RC is then used in Equation (4) where R_{voxel} is the count rate in the voxel.

$$A_{voxel} = \frac{R_{voxel}}{Q \cdot RC} \quad (4)$$

The recovery coefficients for the Jaszczak spheres were then fit to the function given in Equation (5) where $R_{plateau}$, β , and γ are the curve fitted parameters ⁴⁶.

$$RC_{fit} = R_{plateau} - \frac{R_{plateau}}{1 + \left(\frac{V}{\beta}\right)^\gamma} \quad (5)$$

2.4 Monte Carlo dose calculation

An in-house radiopharmaceutical dosimetry platform called RAPID was used to calculate the mean absorbed dose to the tumor structure in the anthropomorphic phantom ³⁰. RAPID utilizes nuclear medicine images to define the radionuclide activity in each voxel and the absorbed dose rate distribution is calculated on the CT which defines the material composition and mass density of the simulation geometry. The acquired SPECT/CT data from the anthropomorphic phantom study was used to calculate a voxel-level dose rate distribution in the phantom. The dose rate in each voxel was then integrated assuming simple exponential decay to produce a total absorbed dose distribution in the phantom.

Three scenarios were considered: i) ground truth using a simulated, idealized, SPECT dataset, ii) SPECT-based dosimetry without RCs, and iii) SPECT-based dosimetry with anthropomorphic phantom informed RCs. The ground truth scenario was run by creating an artificial activity distribution assuming a uniform concentration of 26.2 kBq/cc and 259 kBq/cc in the background and tumor insert respectively. The SPECT data was interpolated to the same resolution as the CT. The dose calculation grid was of dimensions 278 x 280 x 155 voxels with a 0.977x0.977x2.00 mm³ voxel size. The simulation was run with enough particles (8000 decays per voxel) to ensure Monte Carlo statistical uncertainty below 1.0% in the tumor region. Simulations were run on the UW Center for High Throughput Computing (CHTC).

2.5 Uncertainty analysis

Uncertainty analysis was performed according to the recommended EANM guidelines for determining error propagation in radiopharmaceutical dosimetry ⁴⁷.

The fractional uncertainty of the volume determination is given by Equation (6) where a is the voxel size and D is the equivalent sphere diameter of the contoured structure.

$$\frac{u(v)}{v} = 3 \left(\sqrt{\frac{a^2}{6}} \right) \quad (6)$$

The uncertainty of the calibration factor (calculated using Equation (1)) is given by Equation (7) and combines in quadrature two components: the assumed 5% error of the radionuclide calibrator activity measurement ($u(A_{cal})$), and the error of the count rate for the scans to determine the calibration factor $u(C_{ref})$, taken to be the standard deviation of the mean count rate for two timepoints.

$$\left[\frac{u(q)}{q} \right]^2 = \left[\frac{u(A_{cal})}{A_{cal}} \right]^2 + \left[\frac{u(C_{ref})}{C_{ref}} \right]^2 \quad (7)$$

The uncertainty of the expression used to fit the recovery coefficient curve (Equation (5)) is given by Equation (8). \mathbf{g}_c is a matrix of dimensions 4 x 1 containing both the partial derivatives of first order of RC with respect to R_{plateau} , β , γ , and v , and \mathbf{V}_c is a 4 x 4 matrix containing the covariance matrix from the least-squares fitting process and the uncertainty of the volumes, $u^2(v)$.

$$u^2(RC) = \mathbf{g}_c^T \mathbf{V}_c \mathbf{g}_c \quad (8)$$

The uncertainty in the measured mean counts C associated with the accuracy of the VOI definition is given by Equations (9) and (10),

$$\frac{u(C)}{C} = \frac{\varphi}{2RC} \frac{u(v)}{v} \quad (9)$$

$$\varphi = \text{erf}\left(\frac{2r^2}{\sigma\sqrt{2}}\right) - \frac{2\sigma}{r\sqrt{2\pi}} \left[1 - e^{-\frac{2r^2}{\sigma^2}}\right] \quad (10)$$

where r is $D/2$ (the equivalent sphere diameter of the structure) and σ is the standard deviation of the Gaussian point spread function derived from the system spatial resolution, assumed to be 3mm ⁴⁸.

The cumulative activity uncertainties were calculated by adding the system sensitivity, recovery coefficient, and count rate errors in quadrature and subtracting out the covariance of the count rate and recovery coefficient on volume ³⁴. The uncertainty of the activity was estimated using Equation (11).

$$\left[\frac{u(\tilde{A})}{\tilde{A}}\right]^2 = \left[\frac{u(q)}{q}\right]^2 + \left[\frac{u(RC)}{RC}\right]^2 + \left[\frac{u(C)}{C}\right]^2 - \frac{\varphi}{RC^2 v} \frac{\partial RC}{\partial v} u^2(v) \quad (11)$$

3. Results

3.1 Phantom geometry

Figure 2 a-c shows photographs of the head and neck phantom and labels for the fillable and removable inserts. **Figure 2a** shows an image of the phantom assembled and filled with water.

Figure 2b shows the anterior half of the skull insert with the 3D printed tumor volume and parotid glands attached to it by simple fasteners. **Figure 2c** shows a side profile of the phantom depicting the lacrimal glad (integrated into the skull) and the thyroid gland (integrated into the shell).

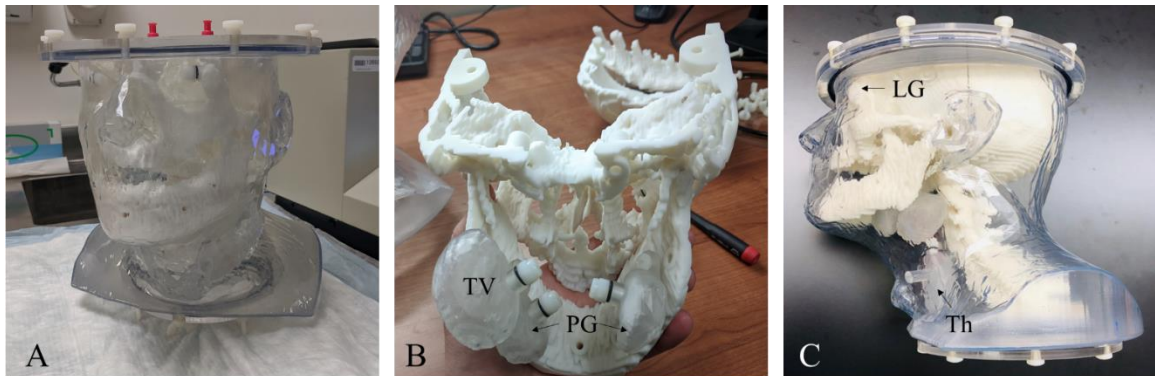


Figure 2: Photographs showing the (a) main chamber (skin), (b) lower jawbone assembly, and (c) compiled head and neck phantom. Labels for the fillable inserts including the tumor volume (TV), parotid gland (PG), lacrimal gland (LG), and thyroid (Th) are superimposed on the photographs.

3.2 Material Properties of Phantom

Figure 3 shows axial, coronal, and sagittal CT slices of the phantom. **Figure 3a** shows an axial slice in which the jaw, spine, parotid glands, and tumor volume is present. **Figure 3b** shows a coronal slice of the phantom in which the skull and the C1-C5 vertebrae are present. **Figure 3c** depicts a sagittal view of the phantom in which the thyroid gland and the parotid gland are present.

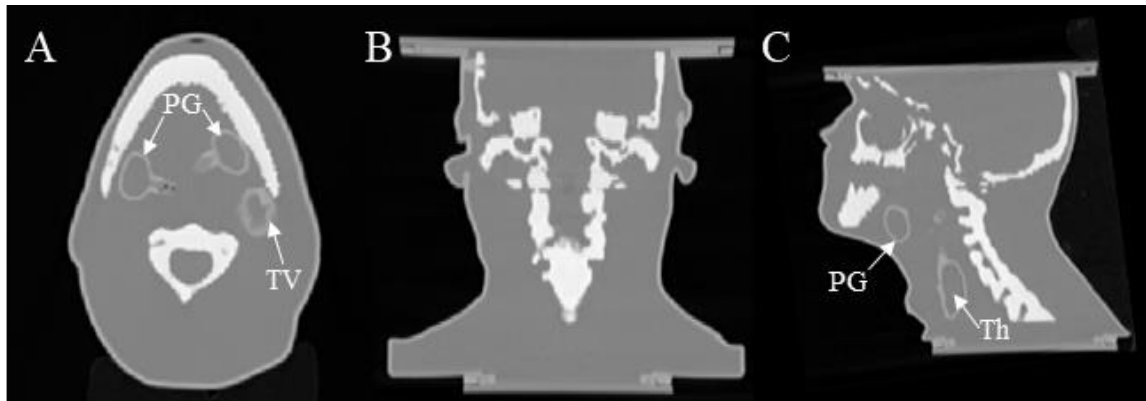


Figure 3: CT scan of phantom showing (a) axial, (b) coronal, (c) sagittal views. Labels for the fillable inserts including the tumor volume (TV), parotid gland (PG), and thyroid (Th) are superimposed on the photographs.

Table 3 provides the radiological properties of the bulk materials. Densities were provided by the manufacturer. The measured HU corresponds to ROIs drawn on bulk portions of the material by the Siemens high-resolution CT scanner. The tabulated attenuation coefficients

are calculated according to the bilinear relationships established by Brown et. al. for ^{131}I and PET⁴⁹ and Kabasakal et. al for ^{177}Lu ⁵⁰.

Table 3: Radiological properties of the bulk materials

Material	Density (g/cc)	Measured HU	Attenuation coefficient (cm ⁻¹)		
			^{177}Lu 50	^{131}I (364 keV)	PET (511 keV)
Accura60	1.21	292.48 +/- 8.57	0.1579	0.1063	0.1068
Somos PerFORM	1.61	876.36 +/- 14.77	0.2137	0.1390	0.1402
Water	1.00	-4.05 +/- 7.95	0.1295	0.0896	0.0896

Figure 4 depicts a portion of the CT calibration curve for the high-resolution CT scanner that the anthropomorphic phantom was scanned in. It also plots the two 3D printed materials alongside the curve in which the clinical calibration curve would slightly overpredict the electron density of the material.

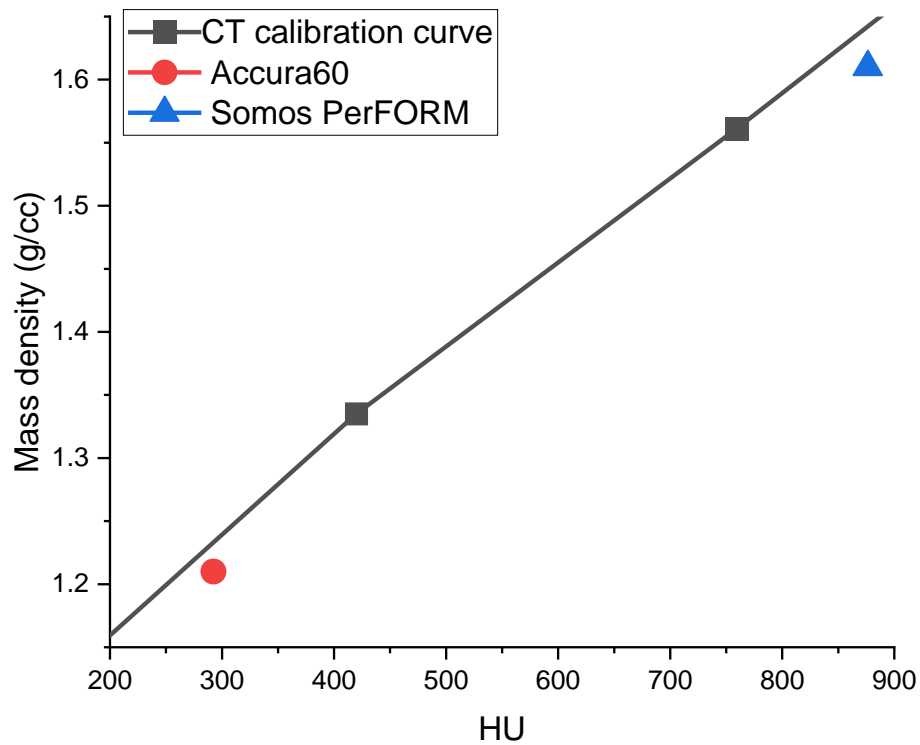


Figure 4: Portion of the CT calibration curve for the Siemens high resolution CT scanner, and the 3D printed materials overlaid

Table 4 shows a comparison between the measured volume of fillable chambers in the phantom and the volume of contours made on a high-resolution CT of the phantom. The maximum relative difference between the measured and contour is -10.07% for the right lacrimal gland which corresponds to an absolute difference of 0.15 ml. The largest absolute difference in volume was for the thyroid gland at 1.35ml. This is likely because it is the most irregularly, aspherical, shaped organ.

Table 4: Comparison of fillable volumes in anthropomorphic phantom (ml)

Fillable void	Measured	DICOM contour	Absolute difference	Percent difference
Parotid_L	8.75	8.44	-0.31	-3.54
Parotid_R	8.39	8.39	0.00	0.01
Lacrimal_L	1.42	1.51	0.09	6.34
Lacrimal_R	1.49	1.34	-0.15	-10.07
Thyroid	14.12	15.47	1.35	9.56
GTV	22.77	22.50	-0.27	-1.19

3.3 Phantom imaging studies

Using Equation (1), the calibration factor (Q) was calculated to be 104.2cps/MBq using RR and 21.4 cps/MBq for non-RR. **Figure 5** shows axial, coronal, and sagittal SPECT/CT slices of the anthropomorphic phantom after SPECT/CT acquisition. For the RR case, the average measured activity in the background and tumor compartments were 24.4 kBq/cc and 127.5 kBq/cc, respectively where the background compartment was a large ROI in the shoulder region containing only water. There was a -6.76% difference between the actual background (26.2 kBq/cc) and measured background. For the non-RR case, the average measured activity in the background and tumor compartments were 24.7 kBq/cc and 110.1 kBq/cc. The difference between the actual background and measured background was -5.81%.

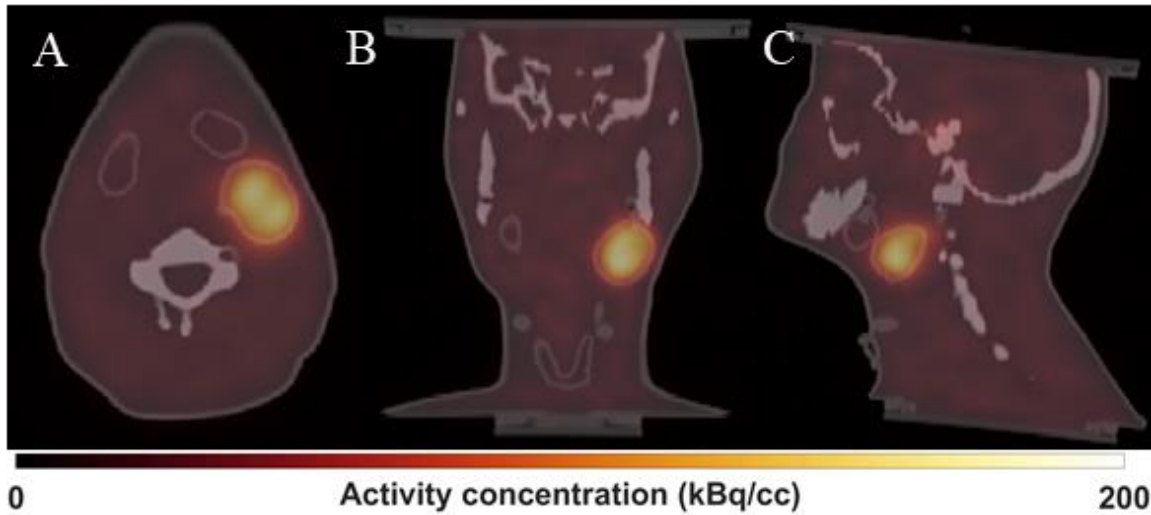


Figure 5: The reconstructed SPECT image and superimposed CT of the I-131 scan showing the (a) axial, (b) coronal, (c) sagittal views of the anthropomorphic phantom.

Figure 6 depicts an axial SPECT/CT slice of the Jaszczak phantom after image acquisition and shows the difference in activity recovered with and without resolution recovery. For the RR case, the average measured activity in the background compartment and 16ml hot sphere compartments were 26.5 kBq/cc and 133.2 kBq/cc, respectively and there was a 2.35% difference between the actual background (25.9 kBq/cc) and measured background. For the non-RR case, the average measured activity in the background compartment and 16ml hot sphere compartments were 26.9 kBq/cc and 109.0 kBq/cc, respectively; and there was a 3.66% difference between the actual background (25.9 kBq/cc) and measured background.

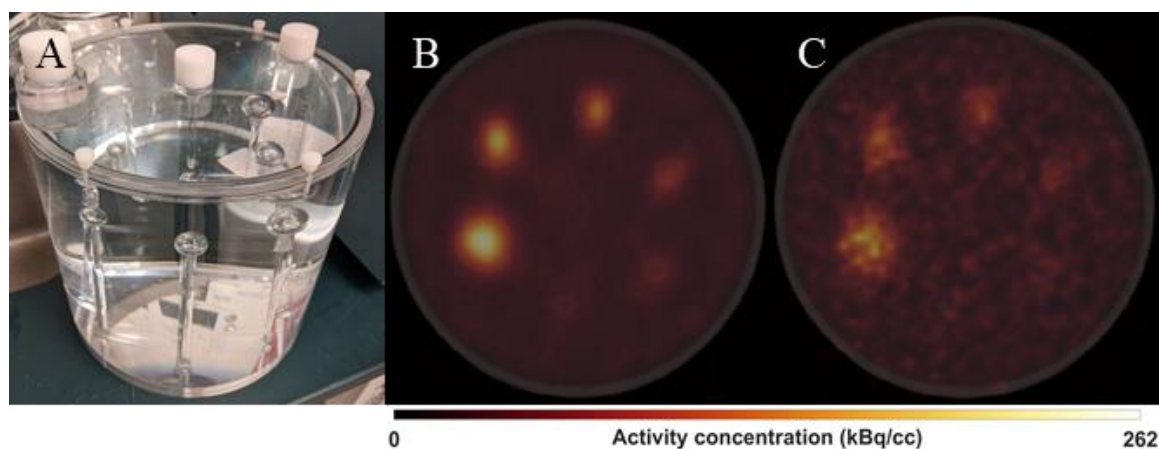


Figure 6: (a) Photograph of the Jaszczak phantom and (b) an axial slice of the reconstructed SPECT image with attenuation and scatter correction and superimposed CT of the I-131 scan with RR and (c) non-RR.

Figure 7 shows the recovery coefficient for the Jaszczak phantom and 3D printed insert as a function of sphere insert size for both the non-RR and RR cases. As the size of the Jaszczak sphere increased, the recovery coefficients increased. Consistent with theory, the curve fit of the Jaszczak spheres in both cases with the non-RR and RR applied demonstrated that the spheres recovered more activity than the aspherical 3D printed volume ³³. The Jaszczak phantom results are fitted to the curvefit as in Equation (5). To calculate the recovery coefficient from the Jaszczak phantom for the anthropomorphic tumor volume, the fitted curve was extrapolated to the volume of the tumor volume. The extrapolated recovery coefficient was greater than that of the 3D printed insert for both the non-RR and RR cases (with RR: 0.536 vs. 0.493, non-RR: 0.445 vs. 0.426 respectively).

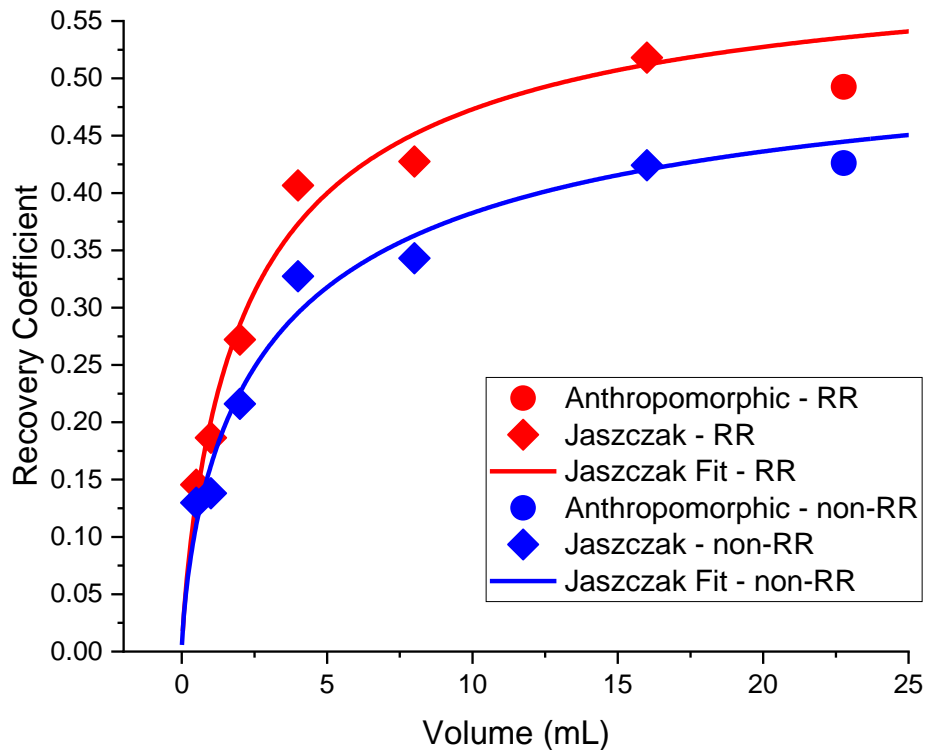


Figure 7: Recovery coefficients calculated for the Jaszczak phantom and 3D printed insert as a function of feature size for both RR and non-RR.

3.4 Monte Carlo dosimetry

Figure 8 shows the difference in the calculated mean tumor dose in comparison to the ground truth scenario with an absorbed dose calculated to be 62.15 Gy. For the RR (non-RR) case, the

mean dose to the tumor was underestimated by 46.8% (53.1%) before applying any RC, underestimated by 4.9% (0.7%) after applying a Jaszczak informed RC, and overestimated by 3.0% (3.0%) after applying the 3D printed insert RC.

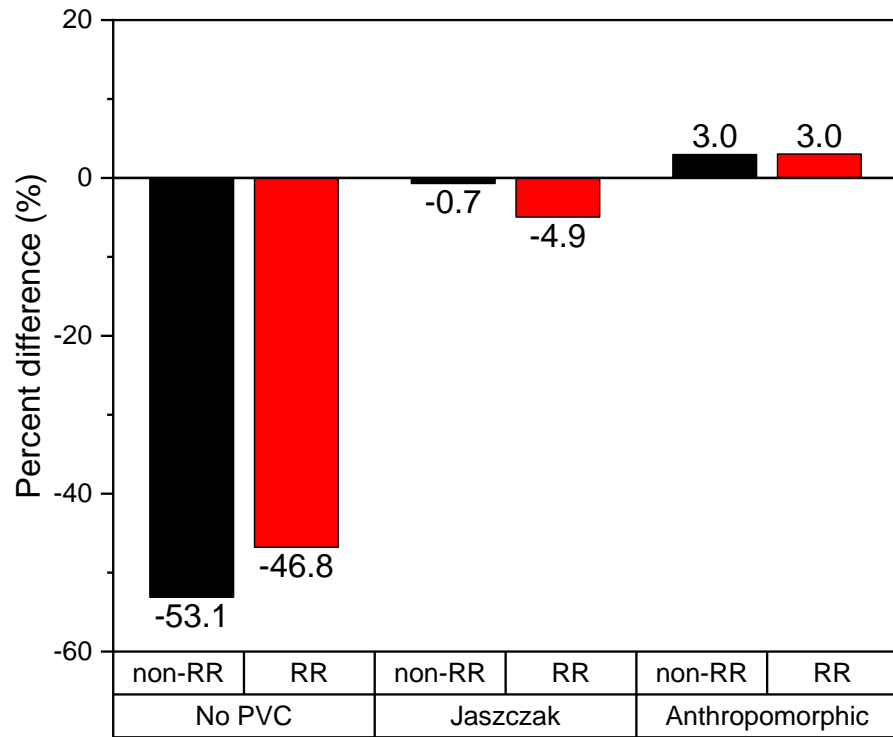


Figure 8: Percent difference in mean absorbed dose to the tumor volume compared to the ground truth (GT) scenario of 62.15 Gy for the scenarios considering RR and PVC.

Figure 9 shows (a) axial, (b) coronal, and (c) sagittal slices of the absolute absorbed dose rate for the ground truth scenario and the respective (d-f) relative percent differences calculated between the ground truth and the SPECT-derived activity distributions for the resolution recovery case.

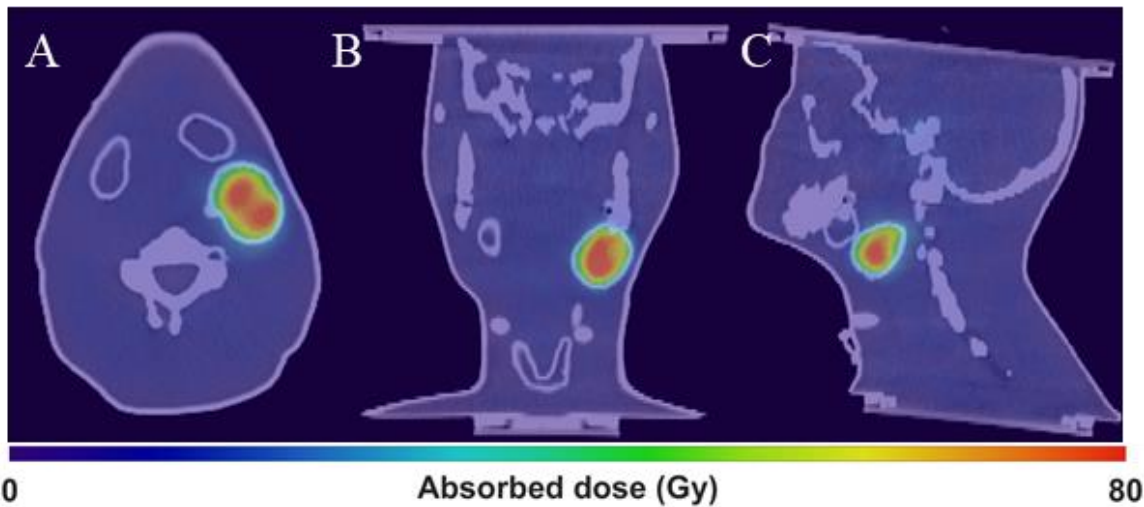


Figure 9: Absolute absorbed dose for the resolution recovery scenario: (a) axial, (b) coronal, and (c) sagittal views.

The calculated uncertainties for the RR case are given in

Figure 10. The largest uncertainties were the mean counts and RC which are dependent on the volume determination and the RC fitting function. The range of uncertainties for volume (17.3% to 54.7%), RC (22.32% to 95.71%), mean counts (13.2% to 106.4%), calibration factor (7.47%), and cumulative activity (25.6% to 113%) were calculated.

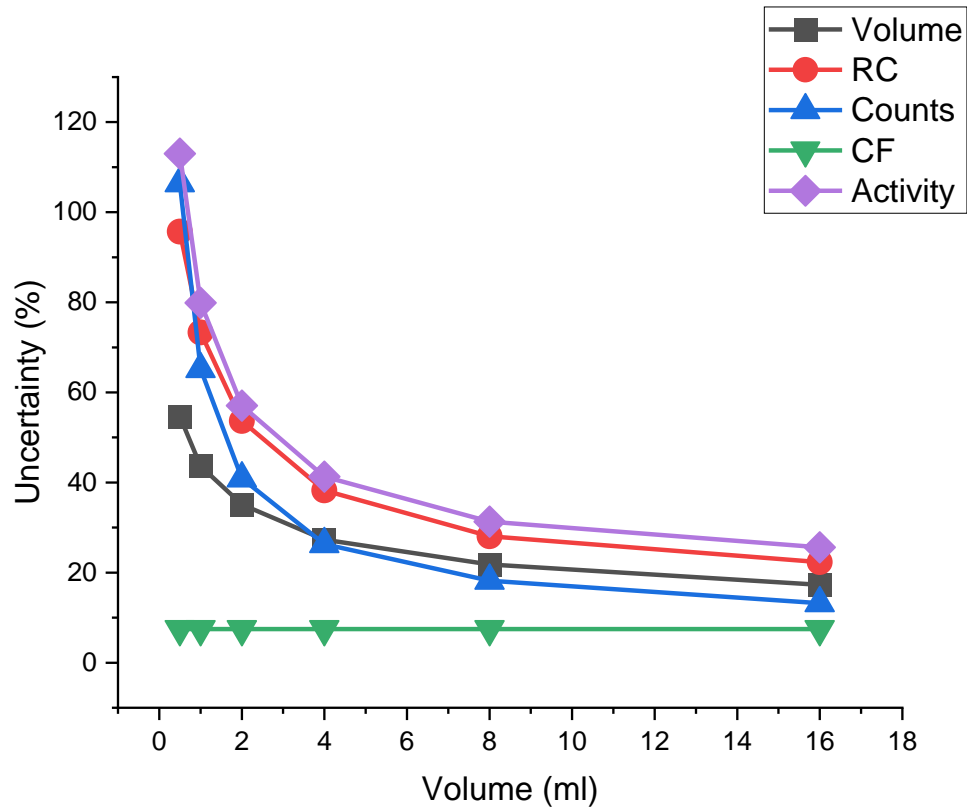


Figure 10: Uncertainties from Jaszczak phantom hot spheres study as a function of sphere volume.

4. Discussion

It was found that, in this study, the Jaszczak based PVC were sufficient to correct the activity distributions. While the Jaszczak-derived RC for the non-RR reconstruction was the most accurate scenario, the anthropomorphic phantom derived RC was most accurate for the RR reconstruction, within 3% of the ground truth. The tumor volume studied was quite spherical in shape and it is possible that for more aspherically shaped volumes, an anthropomorphic RC may be necessary. In the context of uncertainty analysis, the uncertainty in the activity determination was found to be around 25% for the 16 ml Jaszczak sphere, placing all the recovered activity dosimetric results within the calculated error and shows that the RCs determined from the anthropomorphic phantom were dosimetrically similar to those derived from the Jaszczak hot sphere phantom. The uncertainties were even higher (up to >100%) for smaller Jaszczak volumes. This is consistent with previous work in which VOI delineations have a substantial impact on the activity quantification and dose which are especially important for small structures⁴⁸.

Additionally, uncertainties have been reported to be up to 102% for small targets for ^{177}Lu in human clinical trials, placing our results in line with other RPT uncertainties⁵¹.

Because the calibration factor depends on the accuracy of scatter and attenuation correction, and they vary with phantom geometry⁴⁸, the shape of the phantom can directly affect the accuracy of quantifying activity in the background compartment. This may be the reason for the calibration factor slightly underpredicting the activity concentration in the background compartment (an ROI in the shoulder containing only water) of the anthropomorphic phantom. These types of shape-dependent calibration factors have been previously reported^{37,39}. The calibration factor derived from the homogeneous Jaszczak phantom study was used to keep the anthropomorphic phantom study in line with the imaging parameters and recommended guidelines for upcoming clinical trial patient studies³⁴.

In addition to the difference in shape of the phantom's background region, another important distinction of the anthropomorphic phantom is the inclusion of 3D printed bone-mimicking material which more resembles the density and corresponding HU of bones in the head and neck to afford a more realistic dosimetric scenario. The bone-type material was measured to have a bulk HU value of 876.36 and density of 1.61 g/cc which is representative of cortical bone, oftentimes found in the skull. Uncertainties and differences of 3D printed materials have been demonstrated in previous work by Craft et.al⁵². In that work, slight differences in density and composition of printed materials resulted in dosimetric differences for clinical photon and electron beams. In the context of ^{131}I RPT dosimetry, not only are dose computations affected because 3D printed materials may not lie on the CT calibration curve (see **Figure 4**), but CT-based attenuation corrections for image reconstruction may be affected as well. These material property uncertainties could affect the dosimetry and the further characterizing of 3D printed materials should be carefully considered.

RR, the CDR compensation technique included in GE's reconstruction software, Xeleris 4.0^{53,54} was investigated because, in theory, high energy photon emissions of ^{131}I requires modeling of the high energy collimators that inherently reduce spatial resolution due to the collimator geometry. We found that there was only a small difference in the dosimetric results between non-RR and RR; however, utilizing RR increased the spatial accuracy of the activity quantification and has been recommended to be used³⁴. Additionally, the spatial distribution of activity was less clear and difficult to discern the presence of activity in smaller structures (see **Figure 6c**) thus limiting its applicability. The CDR model in Xeleris only models the intrinsic and geometric components of the collimator and neglects the collimator scatter and penetration, which can lead to significant higher count recovery for ^{131}I ³⁴. In addition to using the manufacturer's RR, Monte

Carlo CDR modeling has been studied in previous work to model the CDR explicitly to account for septal penetration and scatter⁵⁵⁵⁶ and should be considered to improve the accuracy of the image reconstruction.

Large dose gradients were present in the RR dosimetry. This is consistent with both spill out due to imaging system limitations and Gibbs ringing artifacts that have been documented when using CDR modeling⁵⁷⁵⁸³⁵. As depicted in relative difference maps in **Figure 11**, there are stark regions of red, indicating that the SPECT image has much higher dose than the corresponding ground truth. This is attributable to those certain structures like bone material and 3D printed material were assumed to be impermeable to water and thus activity was not assigned to them in the ground truth scenario.

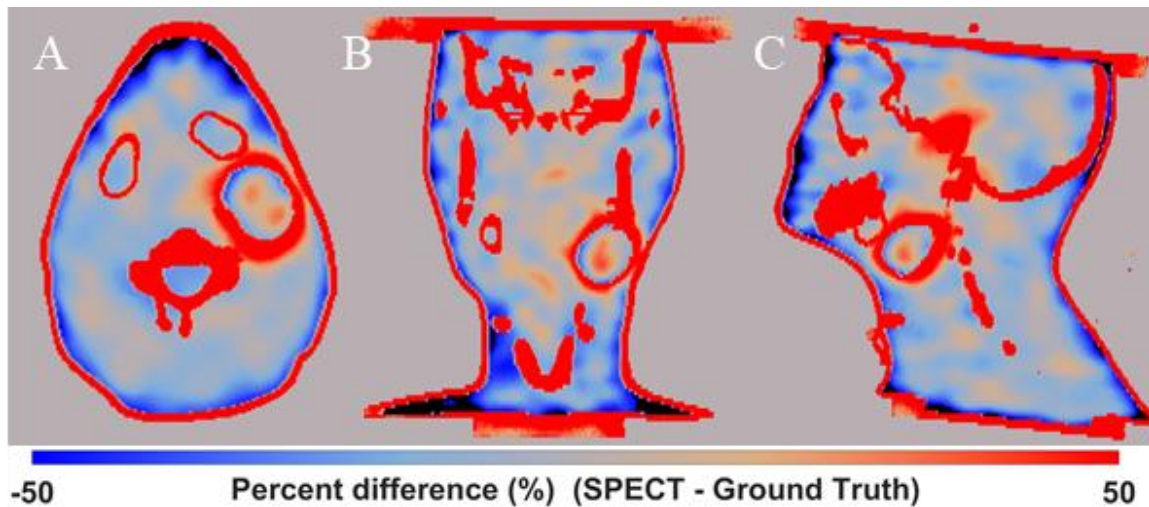


Figure 11: Relative dose differences between the ground truth scenario and SPECT-derived activity distribution with resolution recovery for (a) axial, (b) coronal, and (c) sagittal views.

5. Conclusions

The 3D printed anthropomorphic phantom was created to more accurately represent the geometry and material composition of the head and neck region in comparison to typical non-anthropomorphic Jaszczak-type nuclear medicine phantoms. This phantom was used to evaluate the accuracy of a Monte Carlo, image based, RPT dosimetry workflow in comparison to a ground truth scenario. We investigated the determination of RCs from different phantoms, the impact of CDR modeling, and assessed the uncertainty in the activity determination. After correcting the reconstructed SPECT images using volume-based RCs, the dosimetry workflow was determined to be accurate within the calculated uncertainty. The Jaszczak based PVC were sufficient to correct the activity distributions in this study; however, aspherical volumes may warrant the utilization of anthropomorphic phantom PVC. Further work should characterize the 3D printed

materials rigorously and include Monte Carlo based reconstructions which include more accurate CDR modeling.

Acknowledgements and Financial Disclosure

We would like to thank the UW CHTC for the use of their cluster and their computational support. This project was partially supported by the Morgridge Institute for Research, the Specialized Program of Research Excellence (SPORE) program, through the NIH National Institute for Dental and Craniofacial Research (NIDCR) and National Cancer Institute (NCI), grant P50DE026787, the National Cancer Institute (NCI) Research Project--Cooperative Agreements U01CA233102-01, and the NIH National Cancer Institute (NCI), grant P01CA250972. The content is solely the responsibility of the authors and does not necessarily represent the official views of the NIH.

Disclaimer

BLC is a co-founder of Phantech LLC, a manufacturer of imaging phantoms. BB and JG are co-founders of Voximetry, Inc., a nuclear medicine dosimetry company in Madison, WI.

1. Cognetti DM, Weber RS, Lai SY. Head and neck Cancer an evolving treatment paradigm. *Cancer*. 2008;113(7):1911-1932. doi:10.1002/cncr.23654
2. Forastiere A, Koch W, Trott A, Sidransky D. Head and Neck Cancer. *N Engl J Med*. 2001;345(26):1890-1900. doi:10.1056/NEJMra001375
3. Forastiere A, Weber R, Ang K. Treatment of Head and Neck Cancer. *N Engl J Med*. 2008;358(10):1076-1078. doi:10.1056/NEJMc073274
4. Peters LJ, O'Sullivan B, Giralt J, et al. Critical impact of radiotherapy protocol compliance and quality in the treatment of advanced head and neck cancer: Results from TROG 02.02. *J Clin Oncol*. 2010;28(18):2996-3001. doi:10.1200/JCO.2009.27.4498
5. Pignon JP, Maître A le, Maillard E, Bourhis J. Meta-analysis of chemotherapy in head and neck cancer (MACH-NC): An update on 93 randomised trials and 17,346 patients. *Radiother Oncol*. 2009;92(1):4-14. doi:10.1016/j.radonc.2009.04.014
6. Vokes EE, Weichselbaum RR, Lippman SM, Hong WK. Head and Neck Cancer. *N Engl J Med*. 1993;328(3):184-194. doi:10.1056/NEJM199301213280306
7. Pulte D, Brenner H. Changes in Survival in Head and Neck Cancers in the Late 20th and Early 21st Century: A Period Analysis. *Oncologist*. 2010;15(9):994-1001. doi:10.1634/theoncologist.2009-0289
8. Siegel RL, Miller KD, Jemal A. Cancer statistics, 2015. *CA Cancer J Clin*. 2015;65(1):5-29. doi:10.3322/caac.21254
9. Chen AM, Phillips TL, Lee NY. Practical considerations in the re-irradiation of recurrent and second primary head-and-neck cancer: Who, why, how, and how much? *Int J Radiat Oncol Biol Phys*. 2011;81(5):1211-1219. doi:10.1016/j.ijrobp.2011.06.1998
10. Dawson LA, Myers LL, Bradford CR, et al. Conformal re-irradiation of recurrent and new primary head-and-neck cancer. *Int J Radiat Oncol Biol Phys*. 2001;50(2):377-385. doi:10.1016/S0360-3016(01)01456-0
11. De Crevoisier R, Bourhis J, Domenga C, et al. Full-dose reirradiation for unresectable head and neck carcinoma: Experience at the Gustave-Roussy Institute in a series of 169 patients. *J Clin Oncol*. 1998;16(11):3556-3562. doi:10.1200/JCO.1998.16.11.3556

12. Hehr T, Classen J, Belka C, et al. Reirradiation alternating with docetaxel and cisplatin in inoperable recurrence of head-and-neck cancer: A prospective phase I/II trial. *Int J Radiat Oncol Biol Phys.* 2005;61(5):1423-1431. doi:10.1016/j.ijrobp.2004.08.020
13. Hoebers F, Heemsbergen W, Moor S, et al. Reirradiation for head-and-neck cancer: Delicate balance between effectiveness and toxicity. *Int J Radiat Oncol Biol Phys.* 2011;81(3):e111-e118. doi:10.1016/j.ijrobp.2011.01.004
14. Kasperts N, Slotman B, Leemans CR, Langendijk JA. A review on re-irradiation for recurrent and second primary head and neck cancer. *Oral Oncol.* 2005;41(3):225-243. doi:10.1016/j.oraloncology.2004.07.006
15. Kramer NM, Horwitz EM, Cheng J, et al. Toxicity and outcome analysis of patients with recurrent head and neck cancer treated with hyperfractionated split-course reirradiation and concurrent cisplatin and paclitaxel chemotherapy from two prospective phase I and II studies. *Head Neck.* 2005;27(5):406-414. doi:10.1002/hed.20163
16. Langer CJ, Harris J, Horwitz EM, et al. Phase II Study of Low-Dose Paclitaxel and Cisplatin in Combination With Split-Course Concomitant Twice-Daily Reirradiation in Recurrent Squamous Cell Carcinoma of the Head and Neck: Results of Radiation Therapy Oncology Group Protocol 9911. *J Clin Oncol.* 2007;25(30):4800-4805. doi:10.1200/JCO.2006.07.9194
17. Mendenhall WM, Mendenhall CM, Malyapa RS, Palta JR, Mendenhall NP. Re-irradiation of Head and Neck Carcinoma. *Am J Clin Oncol.* 2008;31(4):393-398. doi:10.1097/COC.0b013e3181637398
18. Nag S, Schuller DE, Martinez-Monge R, Rodriguez-Villalba S, Grecula J, Bauer C. Intraoperative electron beam radiotherapy for previously irradiated advanced head and neck malignancies. *Int J Radiat Oncol Biol Phys.* 1998;42(5):1085-1089. doi:10.1016/S0360-3016(98)00289-2
19. Salama JK, Vokes EE, Chmura SJ, et al. Long-term outcome of concurrent chemotherapy and reirradiation for recurrent and second primary head-and-neck squamous cell carcinoma. *Int J Radiat Oncol Biol Phys.* 2006;64(2):382-391. doi:10.1016/j.ijrobp.2005.07.005

20. Spencer SA, Harris J, Wheeler RH, et al. RTOG 96-10: Reirradiation with concurrent hydroxyurea and 5-fluorouracil in patients with squamous cell cancer of the head and neck. *Int J Radiat Oncol Biol Phys.* 2001;51(5):1299-1304. doi:10.1016/S0360-3016(01)01745-X
21. Stevens KR, Britsch A, Moss WT. High-dose reirradiation of head and neck cancer with curative intent. *Int J Radiat Oncol Biol Phys.* 1994;29(4):687-698. doi:10.1016/0360-3016(94)90555-X
22. Spencer S, Wheeler R, Peters G, et al. Phase 1 trial of combined chemotherapy and reirradiation for recurrent unresectable head and neck cancer. *Head Neck.* 2003;25(2):118-122. doi:10.1002/hed.10178
23. Weichert JP, Clark PA, Kandela IK, et al. Alkylphosphocholine analogs for broad-spectrum cancer imaging and therapy. *Sci Transl Med.* 2014;6(240):240ra75-240ra75. doi:10.1126/scitranslmed.3007646
24. Morris ZS, Weichert JP, Saker J, et al. Therapeutic combination of radiolabeled CLR1404 with external beam radiation in head and neck cancer model systems. In: *Radiotherapy and Oncology.* Vol 116. Elsevier Ireland Ltd; 2015:504-509. doi:10.1016/j.radonc.2015.06.015
25. Grudzinski JJ, Titz B, Kozak K, et al. A phase 1 study of 131I-CLR1404 in patients with relapsed or refractory advanced solid tumors: Dosimetry, biodistribution, pharmacokinetics, and safety. *PLoS One.* 2014;9(11). doi:10.1371/journal.pone.0111652
26. Deming DA, Maher ME, Leystra AA, et al. Phospholipid Ether Analogs for the Detection of Colorectal Tumors. *PLoS One.* 2014;9(10):e109668. doi:10.1371/journal.pone.0109668
27. Lubner SJ, Mullvain J, Perlman S, et al. A Phase 1, Multi-Center, Open-Label, Dose-Escalation Study of 131I-CLR1404 in Subjects with Relapsed or Refractory Advanced Solid Malignancies. *Cancer Invest.* 2015;33(10):483-489. doi:10.3109/07357907.2015.1081691
28. CLR 131 Combined With Radiation for Head and Neck Cancer . <https://clinicaltrials.gov/ct2/show/NCT04105543>. Accessed May 3, 2020.
29. WAHL R. The clinical importance of dosimetry in radioimmunotherapy with

tositumomab and iodine I 131 tositumomab. *Semin Oncol.* 2003;30(2):31-38. doi:10.1016/S0093-7754(03)70055-4

30. Besemer AE, Yang YM, Grudzinski JJ, Hall LT, Bednarz BP. Development and Validation of RAPID: A Patient-Specific Monte Carlo Three-Dimensional Internal Dosimetry Platform. *Cancer Biother Radiopharm.* 2018;33(4):155-165. doi:10.1089/cbr.2018.2451

31. Soret M, Bacharach SL, Buvat I. Partial-volume effect in PET tumor imaging. *J Nucl Med.* 2007;48(6):932-945. doi:10.2967/jnumed.106.035774

32. Hoffman EJ, Huang S-C, Phelps ME. Quantitation in Positron Emission Computed Tomography. *J Comput Assist Tomogr.* 1979;3(3):299-308. doi:10.1097/00004728-197906000-00001

33. Dewaraja YK, Ljungberg M, Koral KF. Monte Carlo evaluation of object shape effects in iodine-131 SPET tumor activity quantification. *Eur J Nucl Med.* 2001;28(7):900-906. doi:10.1007/s002590100551

34. Dewaraja YK, Ljungberg M, Green AJ, et al. MIRD pamphlet No. 24: Guidelines for quantitative ^{131}I SPECT in dosimetry applications. *J Nucl Med.* 2013;54(12):2182-2188. doi:10.2967/jnumed.113.122390

35. Erlandsson K, Buvat I, Pretorius PH, Thomas BA, Hutton BF. A review of partial volume correction techniques for emission tomography and their applications in neurology, cardiology and oncology. *Phys Med Biol.* 2012;57(21). doi:10.1088/0031-9155/57/21/R119

36. Tran-Gia J, Lassmann M. Optimizing image quantification for ^{177}Lu SPECT/CT based on a 3D printed 2-Compartment kidney phantom. *J Nucl Med.* 2018;59(4):616-624. doi:10.2967/jnumed.117.200170

37. Robinson AP, Tipping J, Cullen DM, et al. Organ-specific SPECT activity calibration using 3D printed phantoms for molecular radiotherapy dosimetry. *EJNMMI Phys.* 2016;3(1):12. doi:10.1186/s40658-016-0148-1

38. Woliner-van der Weg W, Deden LN, Meeuwis APW, et al. A 3D-printed anatomical pancreas and kidney phantom for optimizing SPECT/CT reconstruction settings in beta cell imaging using ^{111}In -exendin. *EJNMMI Phys.* 2016;3(1). doi:10.1186/s40658-016-0165-0

39. Price E, Robinson AP, Cullen DM, et al. Improving molecular radiotherapy dosimetry using anthropomorphic calibration. *Phys Medica*. 2019;58(January):40-46. doi:10.1016/j.ejmp.2019.01.013
40. Gear JI, Cummings C, Craig AJ, et al. Abdo-Man: a 3D-printed anthropomorphic phantom for validating quantitative SIRT. *EJNMMI Phys*. 2016;3(1). doi:10.1186/s40658-016-0151-6
41. D'Arienzo M, Pimpinella M, Capogni M, et al. Phantom validation of quantitative Y-90 PET/CT-based dosimetry in liver radioembolization. *EJNMMI Res*. 2017;7. doi:10.1186/s13550-017-0341-9
42. Alqahtani MS, Lees JE, Bugby SL, Samara-Ratna P, Ng AH, Perkins AC. Design and implementation of a prototype head and neck phantom for the performance evaluation of gamma imaging systems. *EJNMMI Phys*. 2017;4(1). doi:10.1186/s40658-017-0186-3
43. Filippou V, Tsoumpas C. Recent advances on the development of phantoms using 3D printing for imaging with CT, MRI, PET, SPECT, and ultrasound. *Med Phys*. 2018;45(9):e740-e760. doi:10.1002/mp.13058
44. Tino R, Yeo A, Leary M, Brandt M, Kron T. A systematic review on 3D-Printed imaging and dosimetry phantoms in radiation therapy. *Technol Cancer Res Treat*. 2019;18:1-14. doi:10.1177/1533033819870208
45. Ang KK, Zhang Q, Rosenthal DI, et al. Randomized Phase III Trial of Concurrent Accelerated Radiation Plus Cisplatin With or Without Cetuximab for Stage III to IV Head and Neck Carcinoma: RTOG 0522. *J Clin Oncol*. 2014;32(27):2940-2950. doi:10.1200/JCO.2013.53.5633
46. Taprogge J, Leek F, Schurrat T, et al. Setting up a quantitative SPECT imaging network for a European multi-centre dosimetry study of radioiodine treatment for thyroid cancer as part of the MEDIRAD project. *EJNMMI Phys*. 2020;7(1). doi:10.1186/s40658-020-00332-9
47. Gear JI, Cox MG, Gustafsson J, et al. EANM practical guidance on uncertainty analysis for molecular radiotherapy absorbed dose calculations. *Eur J Nucl Med Mol Imaging*. 2018;45(13):2456-2474. doi:10.1007/s00259-018-4136-7
48. Gregory RA, Murray I, Gear J, et al. Standardised quantitative radioiodine

SPECT/CT Imaging for multicentre dosimetry trials in molecular radiotherapy. *Phys Med Biol.* 2019;64(24). doi:10.1088/1361-6560/ab5b6c

49. Brown S, Bailey DL, Willowson K, Baldock C. Investigation of the relationship between linear attenuation coefficients and CT Hounsfield units using radionuclides for SPECT. *Appl Radiat Isot.* 2008;66(9):1206-1212. doi:10.1016/j.apradiso.2008.01.002

50. Kabasakal L, AbuQbeitah M, Aygün A, et al. Pre-therapeutic dosimetry of normal organs and tissues of ¹⁷⁷Lu-PSMA-617 prostate-specific membrane antigen (PSMA) inhibitor in patients with castration-resistant prostate cancer. *Eur J Nucl Med Mol Imaging.* 2015;42(13):1976-1983. doi:10.1007/s00259-015-3125-3

51. Finocchiaro D, Gear JI, Fioroni F, et al. Uncertainty analysis of tumour absorbed dose calculations in molecular radiotherapy. *EJNMMI Phys.* 2020;7(1). doi:10.1186/s40658-020-00328-5

52. Craft DF, Kry SF, Balter P, Salehpour M, Woodward W, Howell RM. Material matters: Analysis of density uncertainty in 3D printing and its consequences for radiation oncology. *Med Phys.* 2018;45(4):1614-1621. doi:10.1002/mp.12839

53. Tsui BMW, Hu H-B, Gilland DR, Gullberg GT. Implementation of simultaneous attenuation and detector response correction in SPECT. *IEEE Trans Nucl Sci.* 1988;35(1):778-783. doi:10.1109/23.12831

54. Tsui BMW, Frey EC, Zhao X, Lalush DS, Johnston RE, McCartney WH. The importance and implementation of accurate 3D compensation methods for quantitative SPECT. *Phys Med Biol.* 1994;39(3):509-530. doi:10.1088/0031-9155/39/3/015

55. Dewaraja YK, Ljungberg M, Koral KF. Characterization of scatter and penetration using Monte Carlo simulation in ¹³¹I imaging. *J Nucl Med.* 2000;41(1):123-130.

56. Autret D, Bitar A, Ferrer L, Lisbona A, Bardies M. Monte Carlo modeling of gamma cameras for I-131 imaging in targeted radiotherapy. *Cancer Biother Radiopharm.* 2005;20(1):77-84. doi:10.1089/cbr.2005.20.77

57. Ljungberg M, Sjögren-Gleisner K. The accuracy of absorbed dose estimates in tumours determined by Quantitative SPECT: A Monte Carlo study. *Acta Oncol (Madr).* 2011;50(6):981-989. doi:10.3109/0284186X.2011.584559

58. Kangasmaa T, Sohlberg A, Kuikka JT. Reduction of Collimator Correction Artefacts with Bayesian Reconstruction in Spect. *Int J Mol Imaging*. 2011;2011:1-6. doi:10.1155/2011/630813